Toward Real-Time Monitoring and Control of Single Nanoparticle Properties with a Microbubble Resonator Spectrometer

ACS NANO

Cite This: ACS Nano 2019, 13, 12743−12757

www.acsnano.org

ARTICLE

Toward Real-Time Monitoring and Control of Single Nanoparticle Properties with a Microbubble Resonator Spectrometer

Levi T. Hogan,[†,‡] Erik H. Horak,[†,‡] Jonathan M. Ward,[§] Kassandra A. Knapper,[†] Síle Nic Chormaic,[§] and Randall H. Goldsmith*[,†]

[†]Department of Chemistry, University of Wisconsin-Madison, Madison, Wisconsin 53706, United States

[§]Light-Matter Interactions for Quantum Technologies Unit, Okinawa Institute of Science and Technology Graduate University, Onna, Okinawa 904-0495, Japan

Supporting Information

ABSTRACT: **Optical microresonators have widespread application at the frontiers of nanophotonic technology, driven by their ability to confine light to the nanoscale and enhance light−matter interactions. Microresonators form the heart of a recently developed method for single-particle photothermal absorption spectroscopy, whereby the microresonators act as microscale thermometers to detect the heat dissipated by optically pumped, nonluminescent nanoscopic targets. However, translation of this technology to chemically dynamic systems requires a platform that is mechanically stable, solution compatible, and visibly transparent. We report microbubble absorption spectrometers as a versatile platform that meets these requirements. Microbubbles integrate a two-port microfluidic device within a whispering gallery mode microresonator, allowing for the facile exchange of chemical reagents within the resonator's interior while maintaining a solution-free environment on its exterior. We first leverage these qualities to investigate the photoactivated etching of single gold nanorods by ferric chloride, providing a method for rapid acquisition of spatial and morphological information about nanoparticles as they undergo chemical reactions. We then demonstrate the ability to control nanorod orientation within a microbubble through optically exerted torque, a promising route toward the construction of hybrid photonic-plasmonic systems. Critically, the reported platform advances microresonator spectrometer technology by permitting room-temperature, aqueous experimental conditions, which may be used for time-resolved single-particle experiments on non-emissive, nanoscale analytes engaged in catalytically and biologically relevant chemical dynamics.**

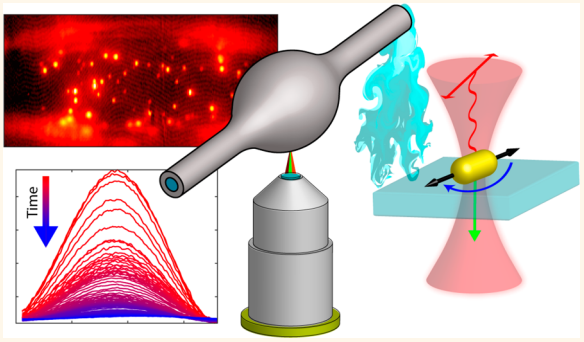

KEYWORDS: *microresonator, single-particle spectroscopy, gold nanorod, photothermal, absorption spectroscopy*

Optical microresonators, devices that confine light to microscopic volumes, have found widespread application within chemistry, biology, physics, and engineering.[1−5] A broad class of optical microresonators, whispering gallery mode (WGM) resonators, have exhibited superb sensitivity including the detection of single nanoparticles,[6,7] single molecules,[8−11] and even single metal ions.[12] However, the ability to perform spectroscopy on adsorbed objects would not only allow for label-free chemical identification but also allow the interrogation of single object properties, free from the static and dynamic blurring of typical ensemble measurements. To this end, we recently employed microtoroid resonators as single-particle absorption spectrometers, whereby the heat dissipated by optically pumped nanoobjects such as gold nanorods (AuNRs),[13−16] carbon nanotubes,[17] or conductive polymers[18] is detected *via* small shifts in the WGM resonance condition. However, to harness the sensitivity of this method for chemically dynamic systems, a platform easily compatible with solution-phase measurements is necessary. Here, we report such a platform, the microbubble resonator, and use it to study the photoactivated chemical etching and reorientation of single AuNRs.

AuNRs[19] have important chemical and biological[20] applications such as bioimaging,[21] treatment of cancer[22,23] and infection,[24] label-free biosensing[25] down to single molecules,[26] surface-enhanced Raman spectroscopy,[27,28] fluorescence enhancement,[29] drug delivery,[30] and light harvesting to drive catalytic reactions.[31] These applications heavily rely on

Received: June 15, 2019
Accepted: October 15, 2019
Published: October 15, 2019

DOI: 10.1021/acsnano.9b04702
ACS Nano 2019, 13, 12743−12757

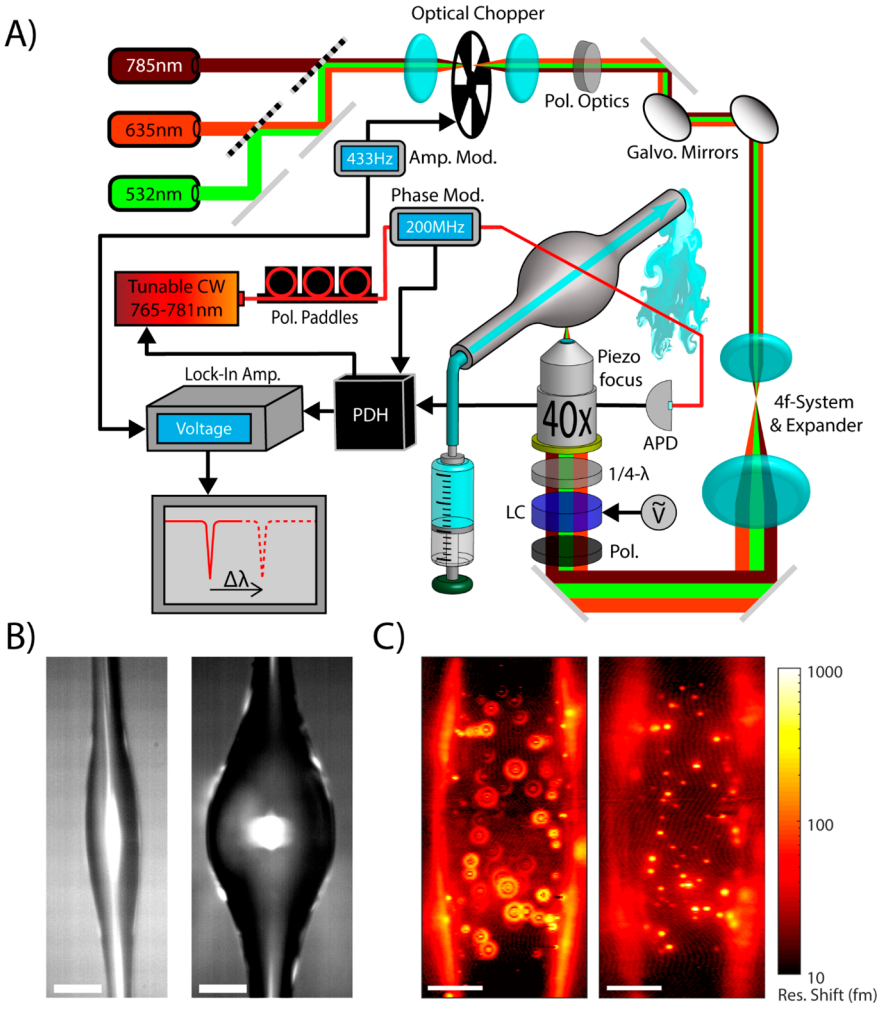

Figure 1. Microbubble absorption spectroscopy. (A) Cartoon of instrumentation. PDH = Pound–Drever–Hall. LC = Liquid crystal. APD = Avalanche photodiode. (B) Optical micrographs of two microbubble resonators with different geometries. Scale bars 20 μm. (C) Photothermal maps of a microbubble resonator similar in geometry to the left microbubble in (B), both out-of-focus (left) and in-focus (right). Scale bars 20 μm.

tuning the morphology-dependent optical features of AuNRs, necessitating precise tailoring of their dimensions. This result can be achieved during AuNR fabrication, where seed-mediated synthesis[32] can often tame the polydispersity that typically plagues samples. However, in many cases, polydisperse AuNR samples are still common, and post-synthetic modifications offer an attractive route to achieve a desired morphology. Furthermore, significant particle-to-particle variations of key optical properties of AuNRs both on surfaces[33] and in solution[34] highlight the heterogeneity within a population of nanoparticles, underscoring the need for single-particle inspection, including during nanoparticle synthesis and modification. A variety of optical methods exist for probing nonluminescent single nanoparticles and molecules *via* photothermal,[35−38] scattering,[39−41] and other techniques.[42−45] Observation of the chemical etching of single AuNRs has recently been accomplished with one-photon luminescence,[46,47] dark-field scattering,[48−54] and liquid transmission electron microscopy (TEM).[55] However, a highly sensitive absorption technique for monitoring such chemical dynamics is needed to compliment these methods and would be extremely valuable for accessing targets that are not luminescent or are too small for scattering experiments. WGM resonators are perfectly poised to fill this gap in methodology.

Various WGM microresonator geometries have been employed for sensing in solution, including microspheres,[9−11] microrings,[5,56] microtoroids,[6,57] microbubbles,[58,59] microdroplets,[60] microtubes,[61] and microbottles.[62,63] In particular, the variations and capabilities of hollow microresonators for sensing have been reviewed in detail elsewhere.[64] To adapt a microresonator for in-solution, visible-wavelength photothermal spectroscopy, three requirements must be met: (i) high sensitivity for interrogating nanoscopic analytes, (ii) resonator transparency at visible wavelengths to mitigate photothermal background, and (iii) robust performance in solution. Employing silica-on-silicon (SiO_2-Si) microtoroids for photothermal spectroscopy, one can resolve attometer shifts of the WGM resonant wavelength from thermal fluxes of target nano-objects.[13] High backgrounds in SiO_2-Si toroids can be mitigated with all-glass microtoroids, which can be used for visible spectroscopy.[15,16] However, immersing a WGM microresonator in water mandates the use of larger microresonators to avoid bending losses,[65] with consequent lower photothermal sensitivity. Furthermore, although tapers[66] and prisms[9] can be optically coupled to WGM microresonators in water,

DOI: 10.1021/acsnano.9b04702
ACS Nano 2019, 13, 12743−12757

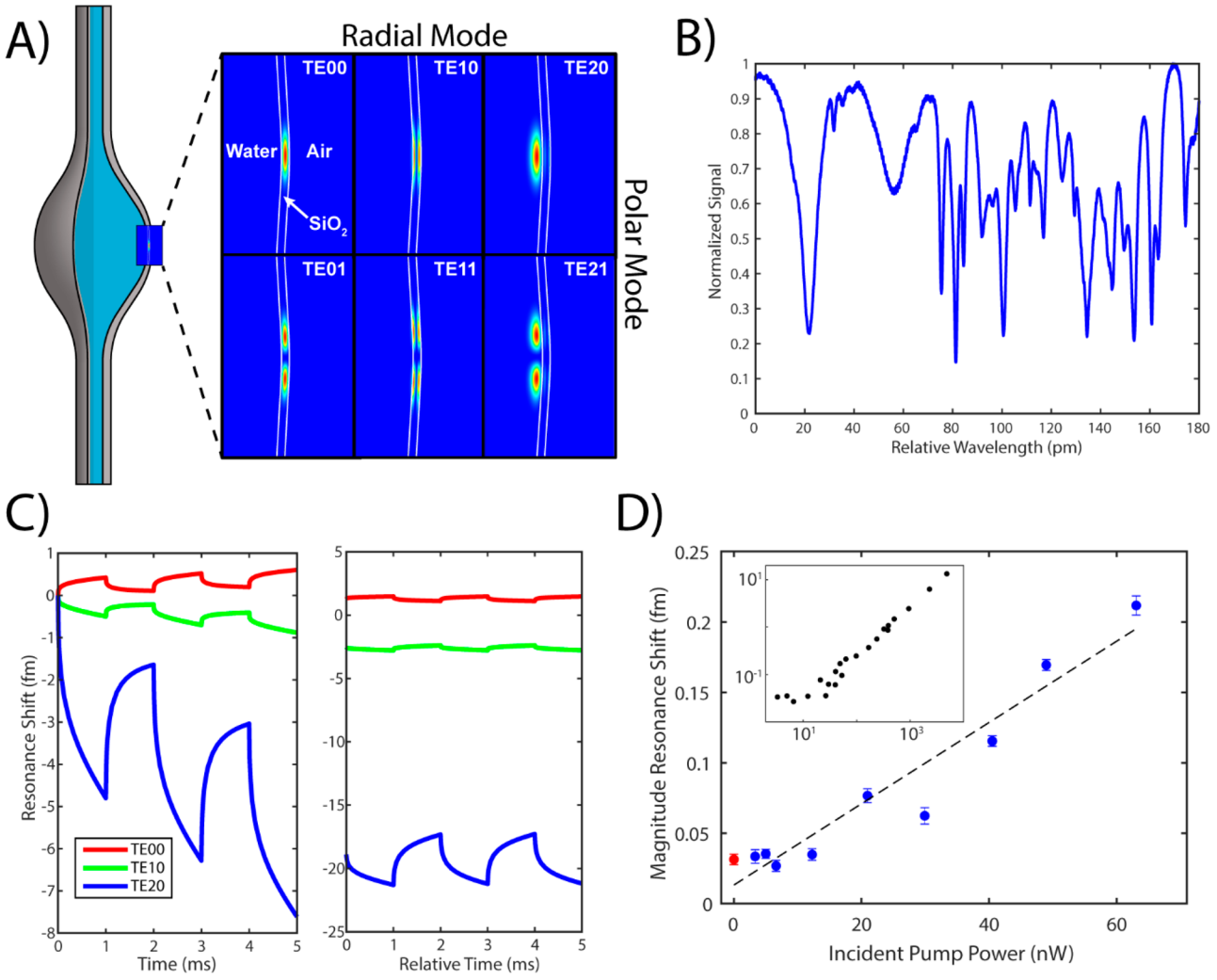

Figure 2. Optical resonances in microbubble resonators. (A) Simulated electric field distributions at 780 nm for first-, second-, and third-order radial modes, for both first- and second-order polar modes. All modes shown are transverse electric (TE). White curves are added to clearly indicate the position of the microbubble walls. (B) A 180 pm span of the mode spectrum of a microbubble resonator. (C) Left: The signal at the beginning of analyte pumping. Right: Signal once the resonator has reached a thermal equilibrium with its surroundings (theoretical). (D) Resonance shift from pumping a single AuNR with the 635 nm beam at decreasing powers (blue points). The red point indicates the signal for pump beam off. The inset is a zoom-out, showing signal linearity over orders of magnitude in pumping power. Further details in main text. Error bars are standard deviation of the mean.

immersion of such couplers in solution may reduce mechanical stability and also result in fouling, particularly as more caustic reagents are employed for chemical studies. Therefore, an alternative platform is preferable for in-solution experiments. The microbubble WGM resonator, Figure 1B, which possesses a hollow, solution-accessible interior, while maintaining an air-glass exterior interface, meets the requirements for in-solution, visible spectroscopy of nanoscopic analytes.

Microbubbles are fabricated from glass capillaries, resulting in low background signals at visible wavelengths, tunable fabrication, and two-port connectivity through which it is easy to flow reagents. Compared to a solid resonator immersed in solution, a microbubble maintains an air−glass interface on its exterior, enabling a higher refractive index contrast and allowing for smaller diameter resonators before bending losses occur. Additionally, the tapered optical fiber used for coupling light into the resonator can approach in air, reducing noise from the instability of coupling in-solution and eliminating solution contamination of the taper. Furthermore, the unique, thin-walled structure of the microbubble allows for high-order optical modes that exist almost entirely within the liquid-core of the resonator, a situation termed the "quasi-droplet regime". Operating in the quasi-droplet regime, microbubbles have proven to be exceptional sensors, most recently for detecting polystyrene nanoparticles in aqueous solution with a sensitivity ~280 times larger than similar experiments using microsphere resonators.[58] Together, these factors make microbubble resonators ideal for time-resolved spectroscopy of single-particle chemical reaction dynamics when exposed to solution. In this paper, we introduce microbubble absorption spectrometers for probing and controlling the chemical and rotational dynamics associated with the photoactivated chemical etching of AuNRs. This platform holds promise for elucidating mechanistic insights into nanoparticle reactions with a method orthogonal to existing techniques that rely on scattering or luminescence and is an attractive candidate for future single-particle and single-molecule studies.

DOI: 10.1021/acsnano.9b04702
ACS Nano 2019, 13, 12743−12757

RESULTS/DISCUSSION

Experimental Design. WGM resonators operate *via* total internal reflection, wherein light propagates around a closed geometric loop, resulting in resonance conditions where only specific wavelengths propagate constructively. WGM resonances are interrogated by the "probe beam", provided by a continuous wave (CW), narrow-line width, tunable laser coupled through a tapered optical fiber[67] (Figure 1A). Transmitted light through the tapered fiber is collected, and the probe beam is actively locked to a resonance by a Pound–Drever–Hall locking system.[6,13,68−70] The hollow core of the microbubble is filled with the desired reagents by attaching the microbubble capillary to a syringe pump. Two microbubbles are pictured in Figure 1B, highlighting the tunability of geometric parameters, and consequent versatility on optofluidic properties.

A second beam, the "pump beam", is focused onto the microbubble surface to excite analytes. CW diode lasers at 532, 635, and 785 nm are coaligned using dichroic mirrors, permitting interrogation at different wavelengths. The linearly polarized pump beam is amplitude modulated at 433 Hz using an optical chopper, encoding the photothermal signal at this frequency and allowing for use of lock-in amplification to drastically lower the experimental noise floor.[13] Two galvanometer mirrors steer the pump beam through a relay lens system to a 40× objective with piezo-controlled focus, providing spatial control of the pump beam on the microbubble resonator. This spatial control is leveraged to photothermally map the interior surface of microbubble resonators, at low resolution for an entire resonator and high resolution for single diffraction-limited objects. Figure 1C shows two photothermal maps of a microbubble resonator at different objective foci, with the out-of-focus map indicating the curvature of the microbubble from the varied PSFs across the map. The polarization angle of the linearly polarized pump beam is rapidly scanned using a voltage-controlled liquid crystal, which is sandwiched between a polarizer and a quarter-waveplate (see Methods). This combination of wavelength, spatial, and polarization control permits thorough characterization of individual analytes bound to the resonator, realized at exquisite sensitivity due to the double-modulation scheme.

Operation of Single-Particle Microresonator Spectrometers. Microresonator sensing schemes generally rely on the reactive mechanism,[10] whereby binding of an analyte imparts a small refractive index change, shifting the resonance wavelength. Instead, microresonator-based photothermal spectroscopy relies on a resonance shift resulting from the heat plume generated by optically pumping a non-emissive object bound to the resonator surface.[17] The temperature rise accompanying this heat plume alters the resonator's refractive index according to its thermo-optic coefficient (dn/dT), changing the WGM optical path length and shifting the resonance condition. The ability to detect this resonance shift is related to the figure of merit Q/V, the ratio of the resonator's quality factor (Q) and mode volume (V). A resonator with minimized absorption, bending, and scattering losses allows photons to repeatedly circulate the resonator, resulting in a high Q, narrow line width resonance. This narrow line width increases the visibility of minute resonance shifts. A smaller resonator with consequent tighter confinement of light produces a smaller V, increasing the overlap between the thermal plume of the analyte and the optical mode. This increased overlap contributes a larger effective refractive index change and thus a larger resonance shift.[17] To properly examine the microbubble photothermal response, we employed finite-element simulations (COMSOL) of both the optical modes and the thermal properties of the microresonator. Simulated optical modes for a particular microbubble geometry are shown in Figure 2A. Varying mode numbers, defined in the traditional spherical geometric indices (polar, azimuthal, and radial, Supporting Information), clearly show the complicated mode structure inherent in the microbubble resonators. This complex mode structure gives rise to several important experimental considerations.

First, the efficient excitation of high-order modes leads to incredibly congested mode spectra. An illustrative 180 pm window of a water-filled microbubble's resonance landscape is shown in Figure 2B. This high mode density stems from the highly prolate resonator geometry lifting the polar mode degeneracy relative to an ideal spherical resonator,[71] leading to varying effective resonator sizes for modes, as well as differing free-spectral ranges.[72] The differing free-spectral ranges cause spectral overlap of modes of different azimuthal mode order,[73] an effect that is compounded by the disparate dielectric environments experienced by different-order radial modes, which have different fractions of the electric field contained in glass, water, and air. Second, the burrowing of higher-order radial modes into the water-filled interior not only changes the effective refractive index of the mode but also yields tremendous variations in dn/dT. This varied dn/dT, which can even switch signs, produces very different thermal responsivities for modes. The combined congested mode spectrum and differential shifting from dn/dT variation amplifies experimental challenges, as photothermal heating or ambient temperature drifting can cause modes to shift through each other. Therefore, modes that are both thermally responsive and spectrally isolable are desirable.

Choosing a high thermal responsivity mode requires delving into the expected thermal response with finite element simulations. As described above, the radial mode order drastically alters the effective dn/dT, as glass has a small positive dn/dT of 9×10^{-6} K^{-1} and water a large negative dn/dT of -91×10^{-6} K^{-1}. Thus, while glass-contained modes in a water-filled resonator offer Q values over 10^6 and show small positive resonance shifts upon heating, higher-order, water-contained modes offer Q values of mid-10^5 and show large negative resonance shifts captured both experimentally (Supporting Information) and in our simulations in Figure 2C. The "shark fin" shape results from the pump beam amplitude modulation. Interestingly, this modulation rides atop a rising baseline magnitude as heat builds over many modulation cycles (left panel) before thermal equilibrium is reached (right panel). This baseline stems from the lack of an effective, proximal heat sink in microbubbles with equilibration reached only after sufficient heat dissipation to the air, yielding a baseline shift about 10 times larger than the modulating shift, both experimentally and theoretically (Supporting Information).

Finding high-order water-contained radial modes to leverage their larger thermal response requires careful consideration of the coupling geometry. Specifically, the tapered fiber diameter[72] greatly impacts mode selectivity through phase matching conditions and evanescent field overlap. By translating along the length of the tapered fiber, this diameter was tuned until these water-contained modes were suitably excited.

DOI: 10.1021/acsnano.9b04702
ACS Nano 2019, 13, 12743−12757

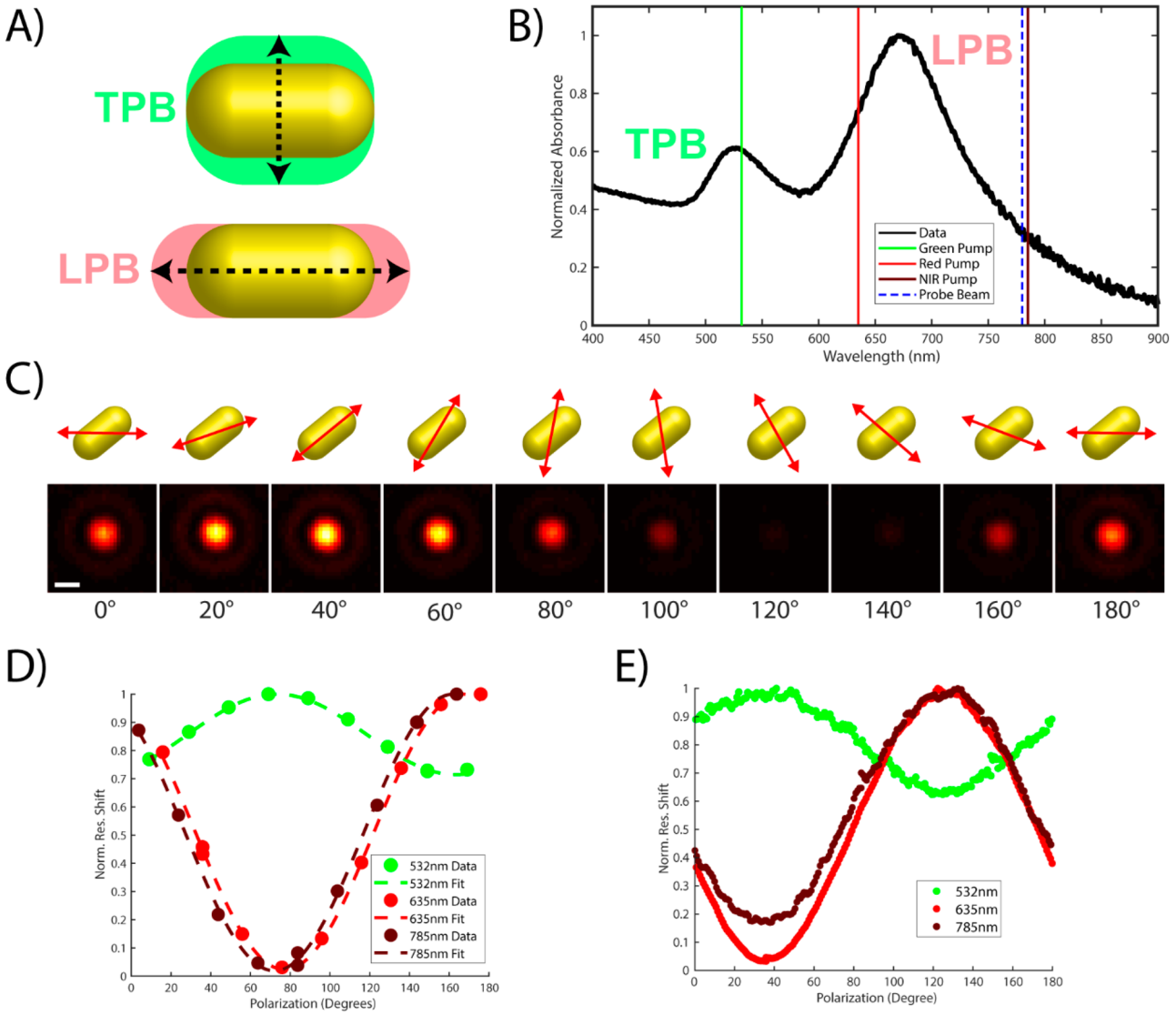

Figure 3. Probing photophysical features of single AuNRs. (A) Cartoon illustrating the photophysical features of a AuNR. LPB = Longitudinal plasmon band. TPB = Transverse plasmon band. (B) Bulk absorption spectrum of AuNRs, with the various laser beams in our experiment indicated by vertical lines. LPB and TPB indicated. (C) Example photothermal maps of a nanorod as pump polarization are varied in increments of 20°, as shown by the red arrow in the cartoon above the photothermal maps. Scale bar 1 μm. (D) Polarization fits for three different pump beams acquired using photothermal mapping. (E) Polarization traces for three different pump beams, acquired by recording photothermal signal as the linear pump polarization is quickly rotated 180° (~10 s).

Then a thermally sensitive and spectrally isolated mode was selected by wavelength scanning. Importantly, the precise identity of this mode was not discerned, precluding direct relation of a resonance shift with an absolute absorption cross-section as in our previous experiments.[13,17] Identification is possible,[74−76] particularly when implementing procedures to simplify the mode structure,[73,77] but difficult in practice and was not pursued here.

Importantly, this lack of mode identification precludes the selection of the maximally thermally responsive mode. While the optimal mode is required for ideal sensor response, use of a less responsive resonance was sufficient for examination of AuNRs. The limit-of-detection of our system was investigated by optically pumping a single AuNR inside a resonator. The photothermal signal, averaged for 30 s with a time constant of 1 s (Figure 2D), was monitored at decreasing powers until it was indistinguishable from the signal obtained with the pump beam blocked. As the inset in Figure 2D shows, the signal remains linear over multiple orders of magnitude, flattening out at low powers as the noise floor is reached. The detection limit for this platform is in the low tens of attometers of wavelength shift (a comparison with microtoroids is made in the Supporting Information). For context, the typical photothermal response of a single AuNR at our pump fluxes is in the range of 10−100 fm, easily resolvable by many orders of magnitude. Additionally, this detection limit surpasses the expected femtometer photothermal shift for measuring a single chromophore.[17] As a first step toward monitoring reaction dynamics of molecules, we show below that microbubbles are well-suited for probing the chemical and spatial dynamics of single AuNRs.

Probing Photophysical Features of Single AuNRs. AuNRs exhibit optical features known as localized surface plasmon resonances (LSPRs), which result from light exciting collective oscillations of conduction band electrons. Two orthogonal LSPRs exist in AuNRs: the longitudinal plasmon

DOI: 10.1021/acsnano.9b04702
ACS Nano 2019, 13, 12743−12757

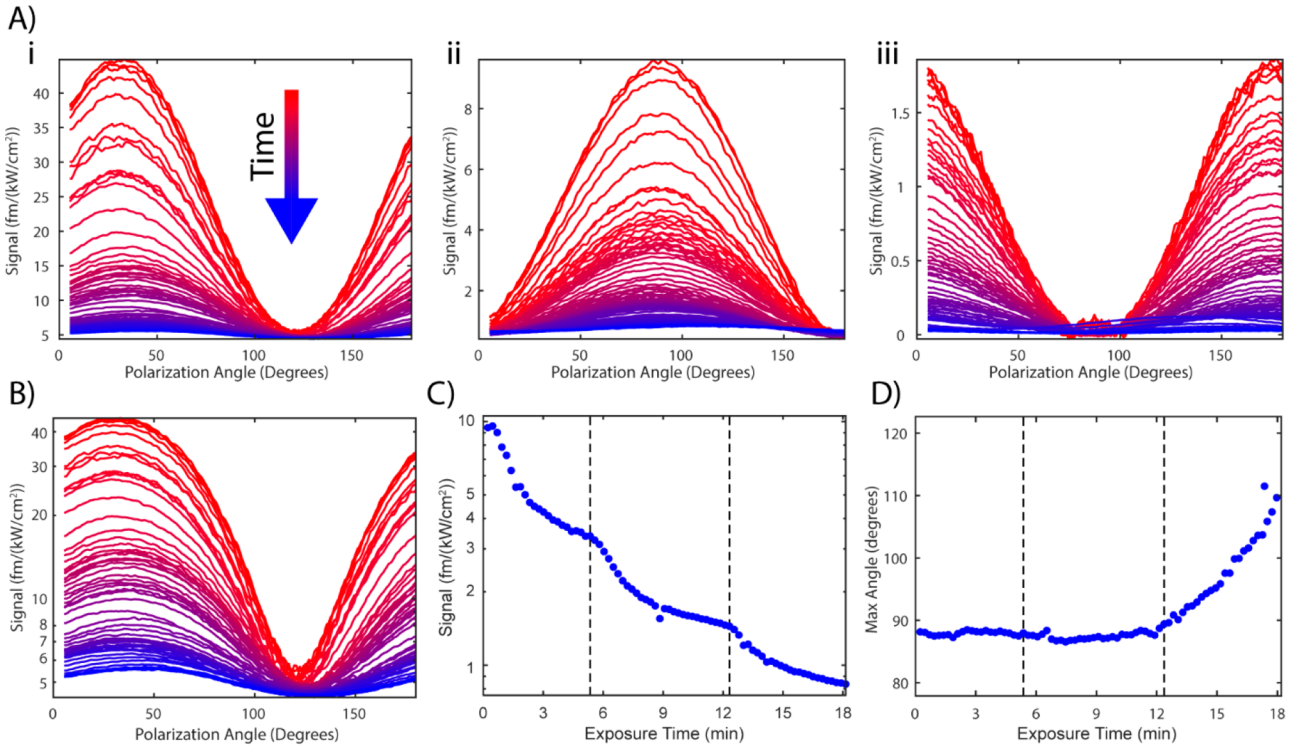

Figure 4. Etching single AuNRs. (A) Reaction series of polarization traces for three difference reactions, progressing in time from red traces to blue traces. Maximum signal is normalized by pump flux. Each trace was taken over the course of 10 s (0.05 s per point, 200 different angles), with a 1 s delay between traces (except when switching power) and 3 s for beam-centering between each trace. (B) The data for reaction (ii), but with signal shown logarithmically. (C) Maximum signal of polarization traces over the course of reaction (ii), showing the decrease in relative absorption cross section at 635 nm. Dashed lines indicate points in time at which pump power was increased. (D) Maximum angle of polarization traces over the course of reaction (ii), showing nanorod orientation. Dashed lines indicate points in time at which pump power was increased. Reaction conditions: dilute aqueous HCl (pH ~ 1.3), room temperature, varied $FeCl_3$ concentrations (i) 1 mM, (ii) 250 μM, (iii) 2 mM. Pump fluxes for reaction (i) were 2.7, 6.7, 11.4, 21.0, and 34.5 kW/cm^2. Pump fluxes for reaction (ii) were 4.1, 11.9, and 35.4 kW/cm^2. Pump fluxes for reaction (iii) were 6.4, 15.9, 31.6, 57.3, and 121 kW/cm^2.

band (LPB) and the transverse plasmon band (TPB), oriented parallel and perpendicular, respectively, to the long axis of the rod (Figure 3A). The LPB is at the longer wavelength in the bulk extinction spectra of the AuNRs used in this report (80 × 40 nm), Figure 3B. These spectral features are probed with the microbubble platform detailed in Figure 1A at the single AuNR level, at specific pump beam wavelengths (solid vertical lines Figure 3B). The LPB central wavelengths will likely be red-shifted compared to the bulk due to interaction with the glass surface.[39,78,79]

After depositing AuNRs inside of a microbubble resonator (Methods), the resonator is photothermally mapped to find objects. To confirm successful deposition of single AuNRs, photothermal maps are acquired with the pump beam, linearly polarized from 0 to 180° (Figure 3C) at three different pump wavelengths. These maps are fit to extract an intensity at each polarization (Methods), shown as data points in Figure 3D. These polarization-dependent intensities are fit (dotted lines) to give a depth-of-modulation, M (Methods). The 635 and 785 nm traces, which probe the LPB, have a value of M close to unity for a single AuNR. A criterion of $M \geq 0.98$ was used for classifying an object as a single AuNR. Small well-ordered aggregates could also exhibit high M values, but these are unlikely due to the presence of CTAB during deposition. Alternatively, a much faster method of probing AuNR orientation is to rapidly rotate the pump beam's linear polarization while centered on an object, and fit the results to extract M. Although this method (Figure 3E) lacks background subtraction, it allows for hundreds of data points to be collected in a few seconds, resulting in quick determination of AuNR orientation and relative absorption cross-section at the pumping wavelength during reactions.

For both of the above polarization methods, the traces for the 635 and 785 nm pump beams align in peak angle (Figure 3D,E) because both of these wavelengths excite the LPB. In contrast, the 532 nm trace has a peak angle orthogonal to the other two traces because this wavelength excites the TPB at a pump polarization orthogonal to the LPB excitation. In addition, the 532 nm trace does not go to zero, because at that wavelength the pump beam is not only pumping the polarization-dependent TPB but also the interband transitions of gold, which are independent of pump beam polarization. Notably, the use of multiple wavelengths means that AuNRs can not only be localized but also studied spectroscopically. Herein, these capabilities are employed to study the etching of AuNRs in real-time.

Selecting an Etchant. The photophysical properties of AuNRs are well understood as a function of geometry,[80] and post-synthetic modifications are extremely useful for exerting control over these properties. Since 2002, when Jana and co-workers observed anisotropic etching of gold spheroids in both cyanide and persulfate solutions,[81] at least 20 other reagents have been reported to etch or accelerate the etching of AuNRs, often with spatial selectivity (see Supporting Information).

DOI: 10.1021/acsnano.9b04702
ACS Nano 2019, 13, 12743−12757

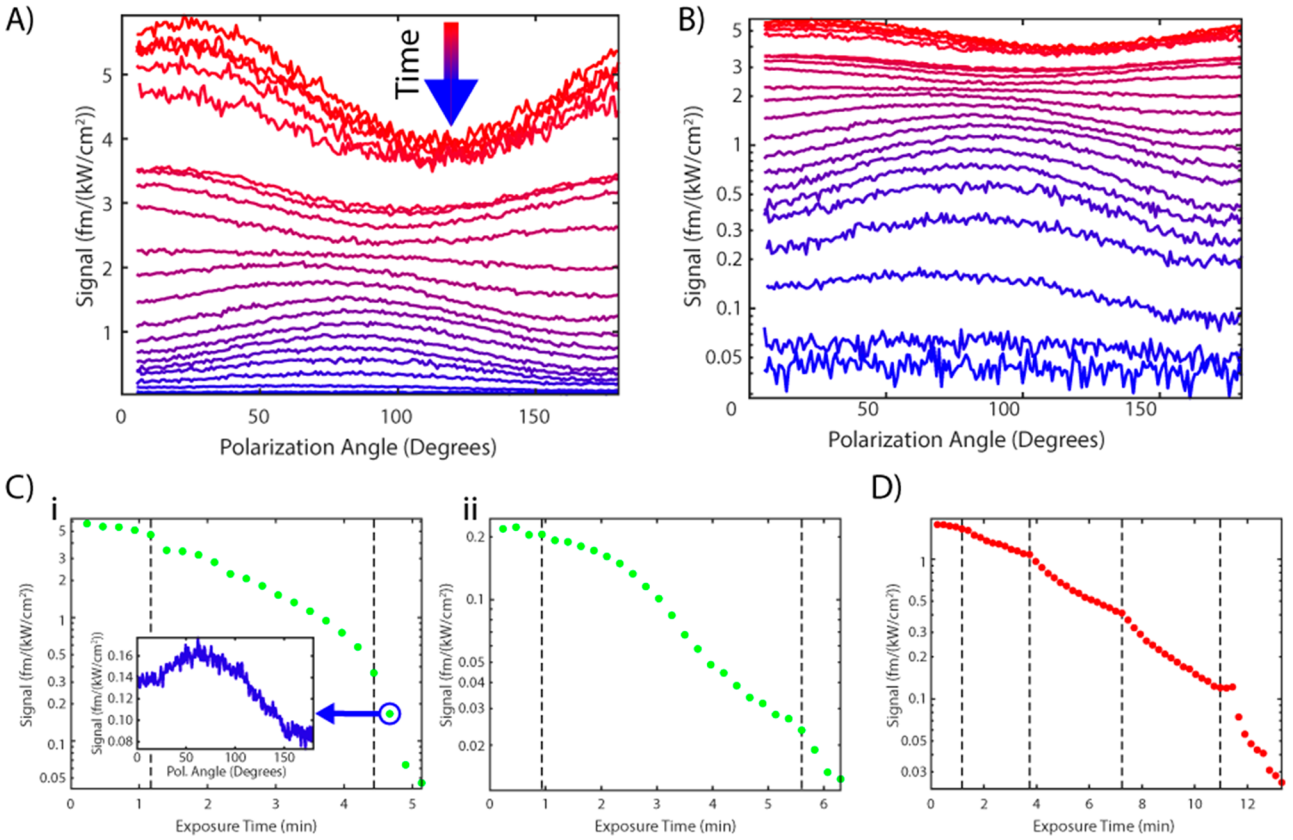

Figure 5. Etching reactions driven at two different pump wavelengths. (A) The reaction of a single AuNR being driven with the 532 nm pump beam, progressing in time from red traces to blue traces. Maximum signal is normalized by pump flux. Each trace was taken over the course of 10 s (0.05 s per point, 200 different angles), with a 1 s delay between traces (except when switching power), and 3 s for beam-centering between each trace. (B) The same data as in (A), but with signal shown logarithmically. (C) (i) Maximum signal of polarization traces for the reaction shown in (A). Polarization trace for indicated data point in inset. (ii) A similar trace for a different nanorod reacted in the same bubble using the 532 nm beam. Dashed lines indicate time points at which pump power was increased. (D) Maximum signal of polarization traces for the reaction of a nanorod in the same bubble, but using the 635 nm pump beam to drive the reaction. Dashed lines indicate time points at which pump power was increased. Reaction conditions: dilute aqueous HCl (pH ~ 1.3), room temperature, 1 mM $FeCl_3$. Pump fluxes for reaction (Ci) were 16.1, 39.2, and 63.3 kW/cm^2. Pump fluxes for reaction (Cii) were 6.4, 31.6, and 57.3 kW/cm^2. Pump fluxes for reaction (D) were 6.4, 15.9, 31.6, 57.3, 121 kW/cm^2.

Such reports include assays for facile detection of analytes at ultralow concentrations in both environmental and biological samples, indicating the utility of morphological control of AuNRs both in-the-field and at points-of-care.

Most of the aforementioned reports used spectrophotometers to study ensembles of AuNRs. Although some studies used TEM intermittently to verify nanorod morphology, this approach is limited in time resolution and generally requires stopping reactions for analysis. Optical monitoring of reactions of single AuNRs can also be accomplished *in situ*. Dark-field spectral imaging has been used to study anisotropic etching of individual AuNRs by hydrogen peroxide,[49] potassium iodide/iodine,[50] and gold(III).[53] In a different experimental design, luminescence was employed to study the cyanide etching of AuNRs.[47] Additionally, dissolution of AuNRs *via* substrate voltage tuning has been monitored using dark-field hyperspectral imaging.[48,54] Perhaps the most commonly reported reagent for etching single AuNRs in recent years is iron(III) chloride, starting with bulk studies in 2009.[82] Since then, $FeCl_3$ etching of single AuNRs has been reported using dark-field monitoring, sometimes utilizing Le Chatlier's principle to drive the reaction.[51,52] Ferric etching of single AuNRs using an electron beam, monitored by liquid-TEM, has also been reported.[55] Excepting the electron beam study, these reports evoked purely chemical mechanisms to explain their reported chemistries. However, the light-induced etching of AuNRs using $FeCl_3$ has also been reported, both in bulk studies[83] and single AuNR experiments using one-photon luminescence.[46] Due to significant interest in ferric etching of AuNRs and the intriguing mechanistic parameter space, $FeCl_3$ was employed for etching in this report.

Single AuNR Reactions. After single AuNRs deposited in the microbubble resonator were identified, they were chemically etched using $FeCl_3$. The etching solution, ranging between 250 μM and 2 mM $FeCl_3$ dissolved in dilute hydrochloric acid (pH ~ 1.3) to prevent hydrolysis of the oxidant, was flowed into the microbubble. Due to differences in sensitivity resulting from microbubble geometries, mode selection, and even nanorod location within the same microbubble, the relative photothermal signals between nanorods cannot be directly compared. However, the relative signal of one AuNR reacting over time, using the same resonance, directly maps onto a change in absorption cross-section of the nanorod at the pump wavelength and thus its etching progress. Conveniently, nanorod etching was found to be photoactivated by the pump beam illumination (discussed

DOI: 10.1021/acsnano.9b04702
ACS Nano 2019, 13, 12743−12757

further below), allowing controlled reaction initiation. The AuNRs were monitored by repeatedly rotating the linearly polarized pump, interrogating the relative absorption and orientation of the AuNR as it is etched. Importantly, before each polarization trace is taken, a beam-centering algorithm is used to mitigate any false signal decrease from spatial drift of the bubble. The centering also serves as a "dosing" period to enable AuNR etching between polarization traces. Each polarization data point required only 50 ms of data acquisition time, suggesting that fast chemical dynamics can be followed with our approach. A further discussion of time resolution and imaging of small gold nanoparticles (AuNPs) is presented below.

Figure 4A(i-iii) features three exemplary traces of a single AuNR reaction (additional examples in the Supporting Information). These three reactions were taken in different microbubbles on different days, confirming reproducibility of the experiment. A logarithmic version of reaction (i) (Figure 4B) readily shows the late stage continued reaction progression along with AuNR rotation. This behavior is better illustrated in the extracted maximum signal and angle traces from reaction (ii) seen in Figure 4C,D, respectively. "Exposure time" refers to the total time that the AuNR has been exposed to the laser beam, which does not include the "switching time" at the dotted lines, where the laser was turned off so that the power could be increased. The reactions slowed as they progressed, as seen by the plateauing effect in the maximum signal. This plateauing is a direct result of the photoactivation mechanism: As a nanorod shrinks, its absorption cross-section decreases, resulting in less light absorption and thus slower etching. This photoactivation is further confirmed by incrementally increasing the pump power (dotted vertical lines), quickening the reactivity before it plateaus once again. Although the three reactions in Figure 4A were taken at ferric chloride concentrations spanning almost an order of magnitude, the time scales of reaction vary by much less (discussion in Supporting Information). It is also evident that AuNRs sometimes rotate as they etch, especially late in reactions, as seen in Figure 4D and discussed later (see Single AuNR Rotations).

A control experiment was performed with a nanorod-containing resonator filled with dilute hydrochloric acid (pH ∼ 1.3) without $FeCl_3$, confirming that the acid alone is not enough to etch the nanorods under illumination. Additionally, when nanorods are left in etching solution for multiple days without laser illumination, they do not observably react, supporting a photoactivated etching mechanism. AuNRs exposed to etching solution for hours within a microbubble, with the probe beam on and locked to water-dominated modes but no pump beam on, also did not undergo significant etching, indicating that the probe beam is not sufficient to drive etching. Therefore, we hypothesize a photoactivated mechanism resulting from hot electrons generated from LPB decay (see Mechanistic Discussion). We also note that, occasionally, nanorods were "impervious" to photoactivated etching, as discussed further in the Supporting Information.

To exemplify the spectroscopic versatility of this platform, nanorod etching was also induced with the 532 nm pump beam. Because this wavelength pumps the TPB (as well as direct interband transitions), nanorod orientation can still be tracked. In Figure 5A, a single AuNR reaction time series is shown for 532 nm-driven (TPB-driven) conditions, with a logarithmic version of the data shown in Figure 5B for clear visualization of late-stage etching data. The polarization traces are conspicuously different than in Figure 4 because of the presence of polarization-independent interband transitions. In Figure 5C, maximum signals are extracted for this reaction and one other TPB-driven reaction in the same resonator. For direct comparison, a different nanorod in the same microbubble was reacted using the 635 nm pump beam (LPB-driven), with the extracted maximum signals shown in Figure 5D (note, this is the same reaction shown in Figure 4A(iii)). Overall, three such reactions were performed for each color in the same resonator to confirm reproducibility (Supporting Information). Although quantitative comparison of reaction rates between experiments is difficult due to the decreasing rate as absorption cross-section diminishes, it is clear from the extracted maximum signals that while the etching rate of the 532 nm-induced reactions is faster than the rate of the 635 nm-induced reactions, it is not multiple orders of magnitude faster, in contrast to previously reported bulk measurements, discussed further below.[83] The shapes of maximum signal traces for the LPB-driven and TPB-driven reactions are noticeably different, with the LPB-driven reactions yielding a concave up shape, and the TPB-driven reactions yielding a concave-down (Figure 5c(i)) or even sigmoidal shape (Figure 5c(ii)).

We also use data from a TPB-driven reaction to discuss imaging of small AuNPs and compare to darkfield microscopy. Typical dark-field techniques can image AuNPs as small as 30 nm in diameter,[84] with more optimized approaches pushing down to 10 nm.[85] The threshold at which the absorption cross-section overtakes the scattering cross-section in magnitude is at a diameter of around 80 nm for gold nanospheres.[39] At diameters of 20 nm, this ratio of $\sigma_{abs}/\sigma_{scat}$ is ∼100.[39] The initial sizes of the AuNRs in this report (approximate volume 4×10^5 nm^2, as calculated for an 80 × 40 nm cylinder) are already well below the volume of an 80 nm nanosphere (2×10^6 nm^2). Furthermore, after etching the AuNR, the volume is much lower, and we can estimate that volume. For this calculation, we use a 532 nm-driven reaction because the TPB is not expected to shift significantly in its center wavelength regardless of whether the etching is isotropic or anisotropic, meaning that the measured signal should scale proportionally with nanorod volume.[39] The inset of Figure 5c(i) shows a polarization trace from late in the reaction, with its corresponding data point indicated. Although later data points show even smaller signals, this data point was selected because the trace still clearly shows the polarization-dependence associated with the TPB. The signal at 180° in the inset is lower than the signal at 0° because the nanorod is reacting rapidly at the high pump flux (as indicated by the slope of Figure 5c(i)). The selected data point has a signal 34 times smaller than the initial signal, equivalent to a volume of 1.2×10^4 nm^2, or a sphere with a diameter of 14 nm. Thus, even with time resolution of 50 ms per point, microbubble spectrometers are well-suited to study AuNPs of a size that is challenging to reach with dark-field measurements. Significant further increases to our sensitivity can be achieved with use of media with higher thermo-optic coefficients[37,86−88] or use of more optimized optical modes (see discussion above).

Mechanistic Discussion. Our proposed mechanism relies on the generation of hot electrons, as in previous reports of photoactivated AuNR etching.[82,89] Interest in such hot carrier chemical processes has exploded in recent years in a variety of applications,[90] especially photocatalysis.[91−93] The mechanisms

DOI: 10.1021/acsnano.9b04702
ACS Nano 2019, 13, 12743−12757

of hot carrier generation and transfer have been extensively studied,[94−97] including efforts toward untangling the contributions of hot carrier effects and photothermal effects in nanoparticle synthesis[98] and plasmonic photocatalysis[99] and mapping hot carrier driven catalytic reactions nanoscopically.[100,101] Although there are still unresolved questions regarding plasmon-driven chemistry, hot carrier transfer can generally be predicted by using an energy overlap model.[102]

In the reported reactions, we expect a nominal temperature rise at the nanorod's surface of <1 K as calculated from the known absorption cross-section and excitation intensity (Supporting Information), meaning that the observed etching mechanism should not be significantly influenced by photothermal heating.[46] With no noticeable dark reaction rate and a photothermal mechanism ruled out, a hot carrier mechanism, whereby the decay of LSPRs or excitation of interband transitions results in hot electrons that can transfer to ferric ions on the nanorod surface, must be invoked to explain the observed reactions. Hot electrons lower the Gibbs free energy of the etching reaction[52] and reduce the thermal activation barrier for electron transfer,[99] thus modifying both the thermodynamics and kinetics of the reaction. Photoexcitation of plasmonic NPs has been experimentally shown to lower the activation enthalpy for transferring electrons from gold nanoparticles to Fe^{3+}[103] and to lower the energy barrier for reaction at the surface of plasmonic NPs by affecting ligand-NP interactions.[104]

When the LSPRs of an AuNR decay, hot electrons are generated from the conduction band of the nanorod. These hot electrons are on average at lower energy than those generated by interband transitions, though a few carriers will be hotter in the LSPR decay case.[83] Although it was previously reported that interband pumping can drive etching orders of magnitude faster than LPB pumping,[83] this was not observed in our reported reactions. CTAB concentration and halide concentration play significant roles in AuNR etching,[82,89] and we attribute this observed discrepancy to different CTAB-mediated mechanisms. Our nanorod deposition procedure likely removes a significant part but not all of the CTAB (see Supporting Information).[105,106] Thus, the AuNRs in our study have significantly lower CTAB coverage than the report where pumping the interband transition resulted in order of magnitude increase in etch rate, where etching occurred in a medium with CTAB concentration greater than the critical micelle concentration (CMC).[83] Ultimately, the reaction relies on ferric ions binding to the nanorod before hot electron transfer can take place. Thus, a plausible mechanism for the reported reactions entails a two-step process, whereby slow ligand exchange of CTAB with Fe^{3+}, or intercalation of the Fe^{3+} through the residual CTAB, is followed by fast photoactivated etching. A relative increase in the rate of the photoactivated step, as seen previously,[83] is then ultimately masked in the observed rate due to the slowness of the first ligand exchange step, as shown Figure 6. In the limit where ligand exchange is slow, increases in the rate of the photoinduced step would give a somewhat muted effect on the overall reaction rate, as observed.

To further understand the shape of the reaction profiles, we modeled the spectral changes of the TPB and LPB for a nanorod being etched for etching schemes ranging from tip-only etching to side-only etching (Supporting Information). Modeling was able to reproduce the concave-up shape observed in the LPB-driven reactions (Figure 4C). However,

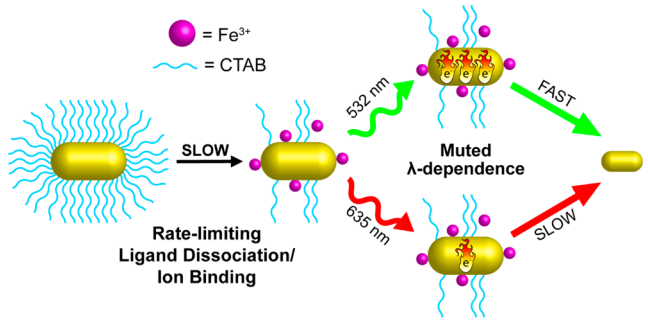

Figure 6. Proposed mechanistic explanation for etching rates. A slow initial step requiring CTAB dissociation before ferric ions can bind determines the overall rate for the reaction, muting the effect of the higher rate for TPB excitation, even though hot electrons are more efficiently generated. Eventually, etching stops when the absorbed light falls below a threshold necessary for hot-electron-driven etching.

no combination of variables was able to capture the concave down or sigmoidal trend seen in some TPB-driven reactions (Figure 5C) or fully reproduce the threshold behavior observed. Thus, with a completely linear reaction mechanism ruled out, we can speculate on possible origins of nonlinearity in the etching mechanism. One possible origin stems from the evolution of nanorod morphology over time. For example, it was observed previously that for certain laser powers, nanorod LPBs would red-shift, then blue-shift.[46] Another possible origin derives from the changing surface concentration of CTAB, with a relatively dense coverage providing competitive inhibition for ferric ion binding at early times but AuNR etching resulting in easier access at later times. Future studies utilizing multiple pump beams could be valuable in studying these complex kinetics, as the evolution of the LPB and TPB spectra would yield important insight into the reaction mechanism. Thus, the reported microbubble platform may be used for spectroscopic, mechanistic studies into the wavelength dependence of hot-carrier-driven chemical dynamics in single plasmonic nanoparticles.

Single AuNR Rotations. Beyond using our microbubble spectrometer to monitor and control nanoparticle size, we can also use it to monitor and control nanoparticle orientation, adding significant utility to the microbubble spectrometer platform. Indicated by the shift in peak polarization during etching reactions (Figures 4 and 5), AuNRs can rotate while etching. Alternatively, active rotation can be induced with the pump beam, allowing for control over nanorod orientation. This control results from the optical torque exerted by linearly polarized light on an anisotropic, absorbing plasmonic structure (Figure 7a), a phenomenon that has been demonstrated experimentally[107] and theoretically[108,109] and is discussed further in the Supporting Information.

Theory predicts that the optical torque acting on the AuNR from the 635 nm pump beam will align the AuNR perpendicular to the polarization of the incident beam. Indeed, this perpendicular alignment is exhibited upon sufficient excitation power. In this way, nanorod orientation can be controlled to within approximately 10° (Figure 7b) as AuNR orientation is stepped through a ∼ 180° rotation. This control was accomplished by monitoring the photothermal signal, dislodging the nanorod with a large optical torque above some threshold incident power, and dithering the polarization until the photothermal signal was minimized at the desired

DOI: 10.1021/acsnano.9b04702
ACS Nano 2019, 13, 12743−12757

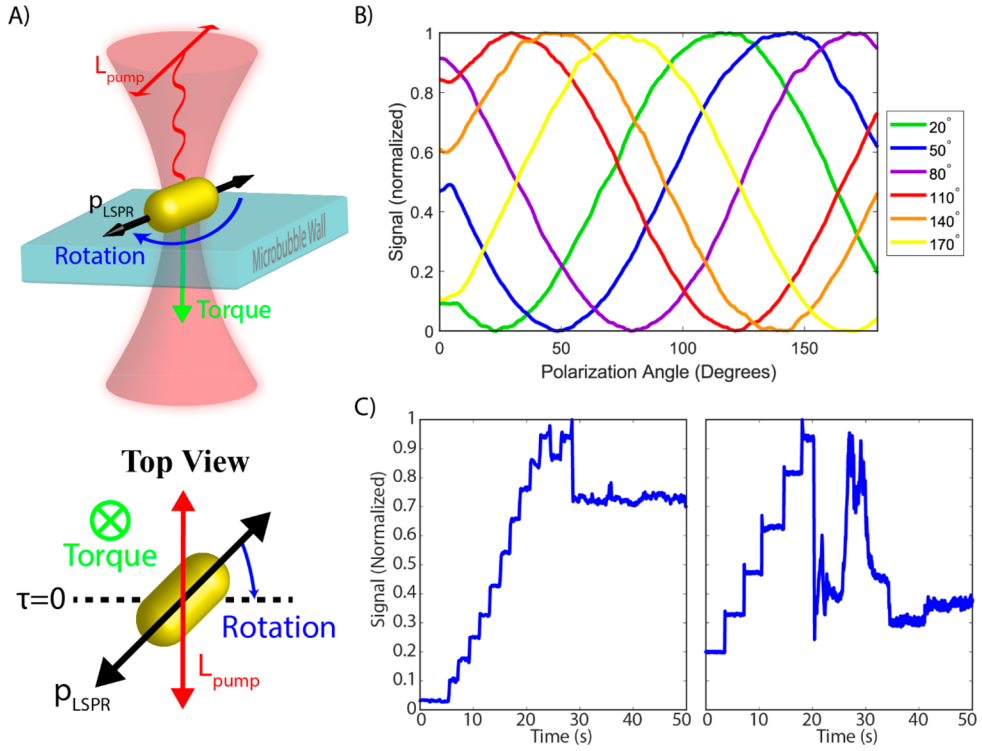

Figure 7. Orientation control of single AuNRs. (A) A cartoon illustrating the optically induced torque that a AuNR experiences under illumination with linearly polarized light, both from side-view (top) and top-view (bottom). (B) A series of pumping experiments showing optical control of nanorod orientation. (C) Trace showing the photothermal signal as two different AuNRs are pumped at increasing laser powers until the AuNRs dislodge slightly from the resonator wall and rotate, eventually settling down off-axis of the polarization.

polarization angle. This thresholding behavior was demonstrated further by a stepwise ramping of the pump laser intensity, resulting in an upward staircase of photothermal signal, until rotation was finally induced. As can be seen in the examples in Figure 7C, two different nanorods required significantly different pump powers to dislodge them from the microbubble surface. Following dislodgment, the signal quickly stabilized to around 70% of the maximum signal for the left nanorod trace, whereas it behaved semistochastically for the right trace, before settling at <40% of the maximum signal. These differences in orientational dynamics highlight the differences in the local environments around the two nanorods, including both Coulombic effects and refractive index differences. These staircase experiments were performed repeatedly for both nanorods in Figure 7C to confirm reproducibility (Supporting Information).

Light-induced rotation during reactions was observed more frequently as AuNR etching progressed. Likely, as Coulombic attractions between the AuNR and the resonator's surface were weakened, hydrodynamic or optical torques were allowed to rotate the AuNR. Although rotation events could be forced in water-filled resonators, higher pump thresholds were generally required, and AuNRs were immune to rotation at powers that would result in rotation in ferric chloride solution. Therefore, it appears that the presence of etchant reduces the Coulombic attraction between nanorods and the resonator wall, possibly through charge screening, permitting facile rotation. Though optical rotation of nanorods has been seen in previous experiments, the coupling between evolving surface chemistry and propensity for rotation has not been explored to our knowledge.

Radiation pressure and optical gradient forces could also influence AuNRs, affecting the rotation power threshold. However, varying the pump beam focus position, which would change forces along the optical axis, did not significantly impact rotation thresholds. Therefore, it appears that the torque described above is the dominant driver of nanorod rotation. Although scattering forces in three-dimensional trapping can orient anisotropic plasmonic nanoparticles parallel to the optical axis of the excitation beam,[110] one would expect this to result in a highly stochastic signal over time in the polarization traces of Figures 3 and 4, as well as a revival of signal upon shutting off and turning back on the pump beam. Such behavior was not observed. Therefore, AuNRs likely remain parallel to the plane of the resonator's surface during rotation, rotating only in two dimensions.

CONCLUSIONS

We have demonstrated microbubble resonators as a robust platform for studying chemical dynamics in solution *via* single-particle absorption spectroscopy. We used a microbubble spectrometer to observe changes in the optical properties of AuNRs as they were controllably etched by ferric chloride *via* a photoinduced mechanism. The sizes of the etched AuNRs push the limit of what can be imaged *via* dark-field scattering. The hypothesis that ligand-exchange-limited etching is the reason for muted wavelength dependence of etching will require more experiments in the future to confirm and understand. Additionally, we monitored and controlled the orientation of the AuNRs using optical torque.

With this demonstration, we lay the groundwork for studying more complex reaction dynamics of single particles and molecules. Thus, this technique provides a complementary

DOI: 10.1021/acsnano.9b04702
ACS Nano 2019, 13, 12743−12757

measurement to the luminescence and dark-field methods previously used to observe similar reactions as reported here. In particular, the demonstrated exquisite sensitivity offers prospects of examining non-emissive objects inaccessible with fluorescence and too small to observe with scattering, which scales as $1/\text{volume}^2$, a more severe penalty than in absorption measurements, which scale more favorably as 1/volume. Furthermore, rotational control could be used to estimate Coulombic forces attaching deposited objects to the resonator, helping to understand the interface between nanoparticles and the surface. This knowledge, combined with structured light-field manipulation of nanoparticles,[111] might be used to arrange arrays of plasmonic nanoparticles as desired. The optical control of plasmonic nanoparticles within a microbubble resonator may allow for in-solution, photonic-plasmonic assembly, and live control of emergent optical properties in such coupled systems. Additionally, by providing a direct thermal readout, our method could be used to untangle the respective contributions of photothermal heating and hot carrier generation for nanoparticle reactions, aiding the design of improved nanocatalysts. Overall, there is a compelling case for the use of microbubbles in materials studies, sensing, and chemical kinetics, and even hybridizing them with plasmonic or acoustic sensing schemes for further applications. Microbubble absorption spectrometers thus hold great potential for pushing the frontiers of absorption spectroscopy at the nanoscale.

METHODS

Microbubble Fabrication. Microbubble resonators were fabricated according to the method reported by Yang and co-workers.[112] First, a glass capillary (Polymicro Technologies, TSP250350) is tapered using a heat-and-pull method, until it is approximately 25 μm in diameter. Next, counter-propagating CO_2 laser beams are focused onto the capillary, while positive pressure is applied from the inside of the capillary using an inert gas. The heat from the laser beams softens the capillary, allowing for the local expansion of the capillary to 50–100 μm in diameter, depending on the experimental parameters. Eventually, radiative cooling from the expanded glass outcompetes the expansion process, and the bubble's size stops increasing. To operate in the quasi-droplet regime, a wall thickness close to the wavelength of the laser beam used for WGM excitation is desirable. Microbubble wall thickness is determined by an equation reported by Henze and co-workers[113] and validated separately by others.[114]

Tapered Optical Fiber Fabrication. Single-mode optical fiber was purchased from Corning (HI 780C). Tapered fibers are made by removing the polymer sheath, cleaning the fiber, and tapering using a heat-and-pull method with a hydrogen torch and motorized actuators (Thorlabs Z825B) until the fiber returns to single-mode, as determined using a 785 nm diode laser (Thorlabs LPS-785-FC) and optical power meter.

Instrumentation for Photothermal Spectroscopy. A tunable, ultranarrow line width, fiber-coupled CW laser (Newport TLB-6712) with a wavelength range of 765–781 nm was used for coupling into resonators. Pound–Drever–Hall (PDH) locking electronics were constructed as previously reported,[13] except for the use of a different voltage-controlled oscillator (Mini Circuits ZX95-310A+) and different lithium niobate phase-modulator (EOSPACE PM-0S5-01-PFA-PFA-765/782). PDH feedback was applied to the tunable laser using high-speed servo controller (Newport LB1005). The optical output from the experiment was collected using an APD (Thorlabs APD430A), and the photothermal signal was extracted using a lock-in amplifier (Ametek 7265). The resulting signal was collected using a data acquisition (DAQ) card (National Instruments BNC2120) for later processing. Custom LabVIEW code was used for instrumentation control. For photothermal mapping, a lock-in time constant of 20 or 50 ms was used. For polarization traces, a lock-in time constant of 50 ms was used.

Diode lasers were used for pump beams, with the wavelengths 532 nm (FTEC2 532–20), 635 nm (FTEC2 635-50), and 785 nm (Thorlabs LPS-785-FC). The pump beam was amplitude modulated using an optical chopper system (Thorlabs MC200B) and steered using galvanometer mirrors (Thorlabs GVS212) run by outputs from the DAQ mentioned above, modified using custom electronics. The pump beam was focused using a piezo-controlled (Thorlabs DRV517) objective (Nikon Plan 40×, 0.65 NA). Pump beam polarization was controlled using a three-optic system, comprised of a linear polarizer (LPVISE100-A), followed by a liquid crystal variable retarder (Thorlabs LCC1423-A, LCC25) with its fast axis set 45° relative to the polarization axis, followed by a zero-order achromatic quarter-wave plate (Thorlabs AQWP05M-600) with its fast axis set 45° relative to the liquid crystal's fast axis. In this design, tuning of the liquid crystal voltage results in a rotation of linearly polarized light at the output of the three-optic system.

Polarization Plots. Shown in Figure 3C,D, AuNRs are first identified by photothermally mapping them at different pump polarizations and processing these maps with a 2D-Gaussian fit, which results in background subtraction. Then, the maximum signals for each plot are together fit to provide a depth-of-modulation (M), using eq 1, which also gives the maximum signal (σ_{max}) plotted in Figure 4C, and the polarization angle of the maximum signal (θ_{max}) plotted in Figure 4D.

$$\sigma(\theta) = \sigma_{max}(1 - M \times \sin^2(\theta - \theta_{max})) \quad (1)$$

For the data in Figure 3E, the liquid crystal is used to rapidly collect many data points that are then fit to eq 1 to obtain M. This method does not include background subtraction.

Bulk/UV–vis Studies. The bulk absorption spectrum in Figure 3B was taken using a UV–visible spectrophotometer (Varian Cary 50). Additionally, studies were conducted to confirm the effects of CTAB concentration and $FeCl_3$ concentration on bulk nanorod etching. The effects of added NaCl were studied to further examine the impacts of chloride concentration. Results and further discussion are in the Supporting Information.

Nanorod Deposition in Microbubbles. All chemicals were purchased through Sigma-Aldrich unless otherwise noted. To deposit nanorods in a microbubble, a 500× serial dilution is made of AuNRs (Nanopartz A12-40-650-CTAB-DIH-1-25, size: 80 × 40 nm, ζ potential: 35 mV, stock pH: 7, stock CTAB concentration: 5 mM) in a solution of 200× diluted HCl and 25 μM CTAB in water. The low CTAB concentration prevents nanorod aggregation during deposition, but keeps the CTAB concentration well below the CMC of ∼1 mM. Dilute hydrochloric acid, which results in a pH of around 1.3, encourages binding of the nanorods on the resonator interior by enhancing Coulombic interactions.[9] For deposition, water is first flowed through the resonator using a syringe pump attached to the first port of the resonator's capillary. Then, dilute HCl is flowed through the resonator to prime the glass surface for deposition. Next, deposition solution is backfilled through the second capillary port, which is cut to a much shorter length to reduce deposition of AuNRs to the capillary's interior walls. Following this, dilute HCl is flowed through the resonator, followed by water, through the first port of the capillary to push out the deposition solution while maintaining a pH gradient. Water is flowed through the resonator for at least several minutes to ensure the removal of nonbound objects and remove excess CTAB from the nanorod surfaces.

Reactions in Microbubbles. All chemicals were purchased from Sigma-Aldrich. Reaction mixtures are made by dissolving and serial diluting ferric chloride hexahydrate in 1/200 dilute hydrochloric acid, resulting in a solution pH of around 1.3. While reaction solution is flowed into the bubble, resonances shift as the refractive index being probed by the WGM changes. Complete filling of the microbubble with reaction mixture is indicated when the resonances have stopped shifting. Following this stabilization, the syringe pump pressure is released, resulting in a microbubble primed for etching experiments.

DOI: 10.1021/acsnano.9b04702
ACS Nano 2019, 13, 12743–12757

ASSOCIATED CONTENT

Supporting Information

The Supporting Information is available free of charge on the ACS Publications website at DOI: 10.1021/acsnano.9b04702.

Geometric parameters of microbubbles, COMSOL simulations, comparison with microtoroids, static offset vs. modulated signal, mode shifting for different *dn/dT* values (experimental), modeling of LPB and TPB during etching, thermal expansion, diagram for mode indices, additional single AuNR etching data, additional rotation data, bulk reaction results, brief discussion on extracting reaction kinetics, background on AuNR etchants, impervious nanorods, discussion of role of CTAB in etching mechanism, estimation of CTAB remaining on AuNRs after deposition, estimation of nanorod temperature increase, theory of nanorod rotation, Matlab code for modeling plasmon changes during etching (PDF)

AUTHOR INFORMATION

Corresponding Author

*E-mail: rhg@chem.wisc.edu.

ORCID

Levi T. Hogan: 0000-0001-5349-8656
Kassandra A. Knapper: 0000-0001-5171-5792
Síle Nic Chormaic: 0000-0003-4276-2014
Randall H. Goldsmith: 0000-0001-9083-8592

Author Contributions

‡These authors contributed equally.

Notes

The authors declare no competing financial interest.

ACKNOWLEDGMENTS

R.H.G. acknowledges support from NIH (GM127957) and NSF (DBI-1556241). S.N.C. and J.M.W. acknowledge support from the Okinawa Institute of Science and Technology Graduate University. We thank J. Millstone and C. Murphy for enlightening conversations about nanoparticle chemistry.

REFERENCES

(1) Heylman, K. D.; Knapper, K. A.; Horak, E. H.; Rea, M. T.; Vanga, S. K.; Goldsmith, R. H. Optical Microresonators for Sensing and Transduction: A Materials Perspective. *Adv. Mater.* **2017**, *29*, 1700037.

(2) Kim, E.; Baaske, M. D.; Vollmer, F. Towards Next-Generation Label-Free Biosensors: Recent Advances in Whispering Gallery Mode Sensors. *Lab Chip* **2017**, *17*, 1190−1205.

(3) Bozzola, A.; Perotto, S.; De Angelis, F. Hybrid Plasmonic-Photonic Whispering Gallery Mode Resonators for Sensing: A Critical Review. *Analyst* **2017**, *142*, 883−898.

(4) Li, Y.; Jiang, X.; Zhao, G.; Yang, L. Whispering Gallery Mode Microresonator for Nonlinear Optics. 2018, arXiv:physics/1809.04878. *arXiv e-Print archive*. https://arxiv.org/abs/1809.04878 (accessed September 13, 2018).

(5) Wade, J. H.; Bailey, R. C. Applications of Optical Microcavity Resonators in Analytical Chemistry. *Annu. Rev. Anal. Chem.* **2016**, *9*, 1−25.

(6) Swaim, J. D.; Knittel, J.; Bowen, W. P. Detection of Nanoparticles with a Frequency Locked Whispering Gallery Mode Microresonator. *Appl. Phys. Lett.* **2013**, *102*, 183106.

(7) Zhi, Y. Y.; Yu, X. C.; Gong, Q. H.; Yang, L.; Xiao, Y. F. Single Nanoparticle Detection Using Optical Microcavities. *Adv. Mater.* **2017**, *29*, 1604920.

(8) Kim, E.; Baaske, M. D.; Schuldes, I.; Wilsch, P. S.; Vollmer, F. Label-Free Optical Detection of Single Enzyme-Reactant Reactions and Associated Conformational Changes. *Sci. Adv.* **2017**, *3*, No. e1603044.

(9) Baaske, M. D.; Foreman, M. R.; Vollmer, F. Single-Molecule Nucleic Acid Interactions Monitored on a Label-Free Microcavity Biosensor Platform. *Nat. Nanotechnol.* **2014**, *9*, 933−939.

(10) Dantham, V. R.; Holler, S.; Barbre, C.; Keng, D.; Kolchenko, V.; Arnold, S. Label-Free Detection of Single Protein Using a Nanoplasmonic-Photonic Hybrid Microcavity. *Nano Lett.* **2013**, *13*, 3347−3351.

(11) Yu, W. Y.; Jiang, W. C.; Lin, Q.; Lu, T. Cavity Optomechanical Spring Sensing of Single Molecules. *Nat. Commun.* **2016**, *7*, 12311.

(12) Baaske, M. D.; Vollmer, F. Optical Observation of Single Atomic Ions Interacting with Plasmonic Nanorods in Aqueous Solution. *Nat. Photonics* **2016**, *10*, 733−739.

(13) Heylman, K. D.; Thakkar, N.; Horak, E. H.; Quillin, S. C.; Cherqui, C.; Knapper, K. A.; Masiello, D. J.; Goldsmith, R. H. Optical Microresonators as Single-Particle Absorption Spectrometers. *Nat. Photonics* **2016**, *10*, 788−795.

(14) Thakkar, N.; Rea, M. T.; Smith, K. C.; Heylman, K. D.; Quillin, S. C.; Knapper, K. A.; Horak, E. H.; Masiello, D. J.; Goldsmith, R. H. Sculpting Fano Resonances to Control Photonic-Plasmonic Hybridization. *Nano Lett.* **2017**, *17*, 6927−6934.

(15) Knapper, K. A.; Heylman, K. D.; Horak, E. H.; Goldsmith, R. H. Chip-Scale Fabrication of High-Q All-Glass Toroidal Microresonators for Single-Particle Label-Free Imaging. *Adv. Mater.* **2016**, *28*, 2945−2950.

(16) Knapper, K. A.; Pan, F.; Rea, M. T.; Horak, E. H.; Rogers, J. D.; Goldsmith, R. H. Single-Particle Photothermal Imaging *via* Inverted Excitation through High-Q All-Glass Toroidal Microresonators. *Opt. Express* **2018**, *26*, 25020−25030.

(17) Heylman, K. D.; Knapper, K. A.; Goldsmith, R. H. Photothermal Microscopy of Nonluminescent Single Particles Enabled by Optical Microresonators. *J. Phys. Chem. Lett.* **2014**, *5*, 1917−1923.

(18) Horak, E. H.; Rea, M. T.; Heylman, K. D.; Gelbwaser-Klimovsky, D.; Saikin, S. K.; Thompson, B. J.; Kohler, D. D.; Knapper, K. A.; Wei, W.; Pan, F.; Gopalan, P.; Wright, J. C.; Aspuru-Guzik, A.; Goldsmith, R. H. Exploring Electronic Structure and Order in Polymers *via* Single-Particle Microresonator Spectroscopy. *Nano Lett.* **2018**, *18*, 1600−1607.

(19) Chen, H. J.; Shao, L.; Li, Q.; Wang, J. F. Gold Nanorods and Their Plasmonic Properties. *Chem. Soc. Rev.* **2013**, *42*, 2679−2724.

(20) Dreaden, E. C.; Alkilany, A. M.; Huang, X. H.; Murphy, C. J.; El-Sayed, M. A. The Golden Age: Gold Nanoparticles for Biomedicine. *Chem. Soc. Rev.* **2012**, *41*, 2740−2779.

(21) Huang, X. H.; El-Sayed, I. H.; Qian, W.; El-Sayed, M. A. Cancer Cell Imaging and Photothermal Therapy in the Near-Infrared Region by Using Gold Nanorods. *J. Am. Chem. Soc.* **2006**, *128*, 2115−2120.

(22) Yin, D. Y.; Li, X. L.; Ma, Y. Y.; Liu, Z. Targeted Cancer Imaging and Photothermal Therapy *via* Monosaccharide-Imprinted Gold Nanorods. *Chem. Commun.* **2017**, *53*, 6716−6719.

(23) Ali, M. R. K.; Wu, Y.; Ghosh, D.; Do, B. H.; Chen, K.; Dawson, M. R.; Fang, N.; Sulchek, T. A.; El-Sayed, M. A. Nuclear Membrane-Targeted Gold Nanoparticles Inhibit Cancer Cell Migration and Invasion. *ACS Nano* **2017**, *11*, 3716−3726.

(24) Meeker, D. G.; Chen, J. Y.; Smeltzer, M. S. Could Targeted, Antibiotic-Loaded Gold Nanoconstructs Be a New Magic Bullet to Fight Infection? *Nanomedicine* **2016**, *11*, 2379−2382.

(25) Cao, J.; Sun, T.; Grattan, K. T. V. Gold Nanorod-Based Localized Surface Plasmon Resonance Biosensors: A Review. *Sens. Actuators, B* **2014**, *195*, 332−351.

(26) Taylor, A. B.; Zijlstra, P. Single-Molecule Plasmon Sensing: Current Status and Future Prospects. *ACS Sens.* **2017**, *2*, 1103−1122.

(27) Lin, K. Q.; Yi, J.; Hu, S.; Liu, B. J.; Liu, J. Y.; Wang, X.; Ren, B. Size Effect on SERS of Gold Nanorods Demonstrated *via* Single Nanoparticle Spectroscopy. *J. Phys. Chem. C* **2016**, *120*, 20806−20813.

DOI: 10.1021/acsnano.9b04702
ACS Nano 2019, 13, 12743−12757

(28) Gao, Z.; Burrows, N. D.; Valley, N. A.; Schatz, G. C.; Murphy, C. J.; Haynes, C. L. In Solution SERS Sensing Using Mesoporous Silica-Coated Gold Nanorods. *Analyst* **2016**, *141*, 5088−5095.
(29) Khatua, S.; Paulo, P. M. R.; Yuan, H. F.; Gupta, A.; Zijlstra, P.; Orrit, M. Resonant Plasmonic Enhancement of Single-Molecule Fluorescence by Individual Gold Nanorods. *ACS Nano* **2014**, *8*, 4440−4449.
(30) Nima, Z. A.; Alwbari, A. M.; Dantuluri, V.; Hamzah, R. N.; Sra, N.; Motwani, P.; Arnaoutakis, K.; Levy, R. A.; Bohliqa, A. F.; Nedosekin, D.; Zharov, V. P.; Makhoul, I.; Biris, A. S. Targeting Nano Drug Delivery to Cancer Cells Using Tunable, Multi-Layer, Silver-Decorated Gold Nanorods. *J. Appl. Toxicol.* **2017**, *37*, 1370−1378.
(31) Wang, F.; Li, C. H.; Chen, H. J.; Jiang, R. B.; Sun, L. D.; Li, Q.; Wang, J. F.; Yu, J. C.; Yan, C. H. Plasmonic Harvesting of Light Energy for Suzuki Coupling Reactions. *J. Am. Chem. Soc.* **2013**, *135*, 5588−5601.
(32) Gole, A.; Murphy, C. J. Seed-Mediated Synthesis of Gold Nanorods: Role of the Size and Nature of the Seed. *Chem. Mater.* **2004**, *16*, 3633−3640.
(33) Baida, H.; Christofilos, D.; Maioli, P.; Crut, A.; Del Fatti, N.; Vallee, F. Surface Plasmon Resonance Spectroscopy of Single Surfactant-Stabilized Gold Nanoparticles. *Eur. Phys. J. D* **2011**, *63*, 293−299.
(34) Li, Z. M.; Mao, W. Z.; Devadas, M. S.; Hartland, G. V. Absorption Spectroscopy of Single Optically Trapped Gold Nanorods. *Nano Lett.* **2015**, *15*, 7731−7735.
(35) Yorulmaz, M.; Nizzero, S.; Hoggard, A.; Wang, L. Y.; Cai, Y. Y.; Su, M. N.; Chang, W. S.; Link, S. Single-Particle Absorption Spectroscopy by Photothermal Contrast. *Nano Lett.* **2015**, *15*, 3041−3047.
(36) Berciaud, S.; Cognet, L.; Tamarat, P.; Lounis, B. Observation of Intrinsic Size Effects in the Optical Response of Individual Gold Nanoparticles. *Nano Lett.* **2005**, *5*, 515−518.
(37) Gaiduk, A.; Yorulmaz, M.; Ruijgrok, P. V.; Orrit, M. Room-Temperature Detection of a Single Molecule's Absorption by Photothermal Contrast. *Science* **2010**, *330*, 353−356.
(38) Chien, M. H.; Brameshuber, M.; Rossboth, B. K.; Schutz, G. J.; Schmid, S. Single-Molecule Optical Absorption Imaging by Nanomechanical Photothermal Sensing. *Proc. Natl. Acad. Sci. U. S. A.* **2018**, *115*, 11150−11155.
(39) Crut, A.; Maioli, P.; Del Fatti, N.; Vallee, F. Optical Absorption and Scattering Spectroscopies of Single Nano-Objects. *Chem. Soc. Rev.* **2014**, *43*, 3921−3956.
(40) Zrimsek, A. B.; Wong, N. L.; Van Duyne, R. P. Single Molecule Surface-Enhanced Raman Spectroscopy: A Critical Analysis of the Bianalyte *versus* Isotopologue Proof. *J. Phys. Chem. C* **2016**, *120*, 5133−5142.
(41) Young, G.; Kukura, P. Interferometric Scattering Microscopy. *Annu. Rev. Phys. Chem.* **2019**, *70*, 301−322.
(42) Celebrano, M.; Kukura, P.; Renn, A.; Sandoghdar, V. Single-Molecule Imaging by Optical Absorption. *Nat. Photonics* **2011**, *5*, 95−98.
(43) Chong, S. S.; Min, W.; Xie, X. S. Ground-State Depletion Microscopy: Detection Sensitivity of Single-Molecule Optical Absorption at Room Temperature. *J. Phys. Chem. Lett.* **2010**, *1*, 3316−3322.
(44) Maley, A. M.; Lu, G. J.; Shapiro, M. G.; Corn, R. M. Characterizing Single Polymeric and Protein Nanoparticles with Surface Plasmon Resonance Imaging Measurements. *ACS Nano* **2017**, *11*, 7447−7456.
(45) Jiang, D.; Jiang, Y. Y.; Li, Z. M.; Liu, T.; Wo, X.; Fang, Y. M.; Tao, N. J.; Wang, W.; Chen, H. Y. Optical Imaging of Phase Transition and Li-Ion Diffusion Kinetics of Single $LiCoO_2$ Nanoparticles During Electrochemical Cycling. *J. Am. Chem. Soc.* **2017**, *139*, 186−192.
(46) Thambi, V.; Kar, A.; Ghosh, P.; Khatua, S. Light-Controlled *In Situ* Bidirectional Tuning and Monitoring of Gold Nanorod Plasmon *via* Oxidative Etching with $FeCl_3$. *J. Phys. Chem. C* **2018**, *122*, 24885−24890.
(47) Carattino, A.; Khatua, S.; Orrit, M. *In Situ* Tuning of Gold Nanorod Plasmon through Oxidative Cyanide Etching. *Phys. Chem. Chem. Phys.* **2016**, *18*, 15619−15624.
(48) Al-Zubeidi, A.; Hoener, B. S.; Collins, S. S. E.; Wang, W.; Kirchner, S. R.; Hosseini Jebeli, S. A.; Joplin, A.; Chang, W.-S.; Link, S.; Landes, C. F. Hot Holes Assist Plasmonic Nanoelectrode Dissolution. *Nano Lett.* **2019**, *19*, 1301−1306.
(49) Cheng, J.; Liu, Y.; Cheng, X. D.; He, Y.; Yeung, E. S. Real Time Observation of Chemical Reactions of Individual Metal Nanoparticles with High-Throughput Single Molecule Spectral Microscopy. *Anal. Chem.* **2010**, *82*, 8744−8749.
(50) Sun, S. S.; Gao, M. X.; Lei, G.; Zou, H. Y.; Ma, J.; Huang, C. Z. Visually Monitoring the Etching Process of Gold Nanoparticles by Ki/I_2 at Single-Nanoparticle Level Using Scattered-Light Dark-Field Microscopic Imaging. *Nano Res.* **2016**, *9*, 1125−1134.
(51) Wang, J.; Zhang, H. Z.; Liu, J. J.; Yuan, D.; Li, R. S.; Huang, C. Z. Time-Resolved Visual Detection of Heparin by Accelerated Etching of Gold Nanorods. *Analyst* **2018**, *143*, 824−828.
(52) Zhang, H. Z.; Li, R. S.; Gao, P. F.; Wang, N.; Lei, G.; Huang, C. Z.; Wang, J. Real-Time Dark-Field Light Scattering Imaging to Monitor the Coupling Reaction with Gold Nanorods as an Optical Probe. *Nanoscale* **2017**, *9*, 3568−3575.
(53) Xie, T.; Jing, C.; Ma, W.; Ding, Z. F.; Gross, A. J.; Long, Y. T. Real-Time Monitoring for the Morphological Variations of Single Gold Nanorods. *Nanoscale* **2015**, *7*, 511−517.
(54) Flatebo, C.; Collins, S. S. E.; Hoener, B. S.; Cai, Y.-y.; Link, S.; Landes, C. F. Electrodissolution Inhibition of Gold Nanorods with Oxoanions. *J. Phys. Chem. C* **2019**, *123*, 13983−13992.
(55) Ye, X. C.; Jones, M. R.; Frechette, L. B.; Chen, Q.; Powers, A. S.; Ercius, P.; Dunn, G.; Rotskoff, G. M.; Nguyen, S. C.; Adiga, V. P.; Zettl, A.; Rabani, E.; Geissler, P. L.; Alivisatos, A. P. Single-Particle Mapping of Nonequilibrium Nanocrystal Transformations. *Science* **2016**, *354*, 874−877.
(56) Sun, Y. Z.; Fan, X. D. Optical Ring Resonators for Biochemical and Chemical Sensing. *Anal. Bioanal. Chem.* **2011**, *399*, 205−211.
(57) Lu, T.; Lee, H.; Chen, T.; Herchak, S.; Kim, J. H.; Fraser, S. E.; Flagan, R. C.; Vahala, K. High Sensitivity Nanoparticle Detection Using Optical Microcavities. *Proc. Natl. Acad. Sci. U. S. A.* **2011**, *108*, 5976−5979.
(58) Ward, J. M.; Yang, Y.; Lei, F. C.; Yu, X. C.; Xiao, Y. F.; Nic Chormaic, S. Nanoparticle Sensing Beyond Evanescent Field Interaction with a Quasi-Droplet Microcavity. *Optica* **2018**, *5*, 674−677.
(59) Barucci, A.; Berneschi, S.; Giannetti, A.; Baldini, F.; Cosci, A.; Pelli, S.; Farnesi, D.; Righini, G. C.; Soria, S.; Conti, G. N. Optical Microbubble Resonators with High Refractive Index Inner Coating for Bio-Sensing Applications: An Analytical Approach. *Sensors* **2016**, *16*, 1992.
(60) Giorgini, A.; Avino, S.; Malara, P.; De Natale, P.; Gagliardi, G. Liquid Droplet Microresonators. *Sensors* **2019**, *19*, 473.
(61) Madani, A.; Harazim, S. M.; Quinones, V. A. B.; Kleinert, M.; Finn, A.; Naz, E. S. G.; Ma, L. B.; Schmidt, O. G. Optical Microtube Cavities Monolithically Integrated on Photonic Chips for Optofluidic Sensing. *Opt. Lett.* **2017**, *42*, 486−489.
(62) Han, K. W.; Kim, J.; Bahl, G. High-Throughput Sensing of Freely Flowing Particles with Optomechanofluidics. *Optica* **2016**, *3*, 585−591.
(63) Stoian, R.-I.; Bui, K. V.; Rosenberger, A. Silica Hollow Bottle Resonators for Use as Whispering Gallery Mode Based Chemical Sensors. *J. Opt.* **2015**, *17*, 125011.
(64) Ward, J. M.; Dhasmana, N.; Nic Chormaic, S. Hollow Core, Whispering Gallery Resonator Sensors. *Eur. Phys. J.: Spec. Top.* **2014**, *223*, 1917−1935.
(65) Kippenberg, T. J.; Spillane, S. M.; Vahala, K. J. Demonstration of Ultra-High-Q Small Mode Volume Toroid Microcavities on a Chip. *Appl. Phys. Lett.* **2004**, *85*, 6113−6115.
(66) Armani, A. M.; Vahala, K. J. Heavy Water Detection Using Ultra-High-Q Microcavities. *Opt. Lett.* **2006**, *31*, 1896−1898.

DOI: 10.1021/acsnano.9b04702
ACS Nano 2019, 13, 12743−12757

(67) Armani, D. K.; Kippenberg, T. J.; Spillane, S. M.; Vahala, K. J. Ultra-High-Q Toroid Microcavity on a Chip. *Nature* **2003**, *421*, 925−928.
(68) Black, E. D. An Introduction to Pound-Drever-Hall Laser Frequency Stabilization. *Am. J. Phys.* **2001**, *69*, 79−87.
(69) Barnes, J. A.; Gagliardi, G.; Loock, H. P. Absolute Absorption Cross-Section Measurement of a Submonolayer Film on a Silica Microresonator. *Optica* **2014**, *1*, 75−83.
(70) Carmon, T.; Kippenberg, T. J.; Yang, L.; Rokhsari, H.; Spillane, S.; Vahala, K. J. Feedback Control of Ultra-High-Q Microcavities: Application to Micro-Raman Lasers and Microparametric Oscillators. *Opt. Express* **2005**, *13*, 3558−3566.
(71) Murugan, G. S.; Petrovich, M. N.; Jung, Y.; Wilkinson, J. S.; Zervas, M. N. Hollow-Bottle Optical Microresonators. *Opt. Express* **2011**, *19*, 20773−20784.
(72) Nasir, M. N. M.; Murugan, G. S.; Zervas, M. N. Spectral Cleaning and Output Modal Transformations in Whispering-Gallery-Mode Microresonators. *J. Opt. Soc. Am. B* **2016**, *33*, 1963−1970.
(73) Ding, M.; Murugan, G. S.; Brambilla, G.; Zervas, M. N. Whispering Gallery Mode Selection in Optical Bottle Microresonators. *Appl. Phys. Lett.* **2012**, *100*, 081108.
(74) Schunk, G.; Furst, J. U.; Fortsch, M.; Strekalov, D. V.; Vogl, U.; Sedlmeir, F.; Schwefel, H. G. L.; Leuchs, G.; Marquardt, C. Identifying Modes of Large Whispering-Gallery Mode Resonators from the Spectrum and Emission Pattern. *Opt. Express* **2014**, *22*, 30795−30806.
(75) Ward, J. M.; Yang, Y.; Nic Chormaic, S. Highly Sensitive Temperature Measurements with Liquid-Core Microbubble Resonators. *IEEE Photonics Technol. Lett.* **2013**, *25*, 2350−2353.
(76) Hall, J. M. M.; Francois, A.; Afshar, V. S.; Riesen, N.; Henderson, M. R.; Reynolds, T.; Monro, T. M. Determining the Geometric Parameters of Microbubble Resonators from Their Spectra. *J. Opt. Soc. Am. B* **2017**, *34*, 44−51.
(77) Murugan, G. S.; Wilkinson, J. S.; Zervas, M. N. Selective Excitation of Whispering Gallery Modes in a Novel Bottle Microresonator. *Opt. Express* **2009**, *17*, 11916−11925.
(78) Davletshin, Y. R.; Lombardi, A.; Cardinal, M. F.; Juve, V.; Crut, A.; Maioli, P.; Liz-Marzan, L. M.; Vallee, F.; Del Fatti, N.; Kumaradas, J. C. A Quantitative Study of the Environmental Effects on the Optical Response of Gold Nanorods. *ACS Nano* **2012**, *6*, 8183−8193.
(79) Ni, W. H.; Chen, H. J.; Kou, X. S.; Yeung, M. H.; Wang, J. F. Optical Fiber-Excited Surface Plasmon Resonance Spectroscopy of Single and Ensemble Gold Nanorods. *J. Phys. Chem. C* **2008**, *112*, 8105−8109.
(80) Park, K.; Biswas, S.; Kanel, S.; Nepal, D.; Vaia, R. A. Engineering the Optical Properties of Gold Nanorods: Independent Tuning of Surface Plasmon Energy, Extinction Coefficient, and Scattering Cross Section. *J. Phys. Chem. C* **2014**, *118*, 5918−5926.
(81) Jana, N. R.; Gearheart, L.; Obare, S. O.; Murphy, C. J. Anisotropic Chemical Reactivity of Gold Spheroids and Nanorods. *Langmuir* **2002**, *18*, 922−927.
(82) Zou, R. X.; Guo, X.; Yang, J.; Li, D. D.; Peng, F.; Zhang, L.; Wang, H. J.; Yu, H. Selective Etching of Gold Nanorods by Ferric Chloride at Room Temperature. *CrystEngComm* **2009**, *11*, 2797−2803.
(83) Zhao, J.; Nguyen, S. C.; Ye, R.; Ye, B. H.; Weller, H.; Somorjai, G. A.; Alivisatos, A. P.; Toste, F. D. A Comparison of Photocatalytic Activities of Gold Nanoparticles Following Plasmonic and Interband Excitation and a Strategy for Harnessing Interband Hot Carriers for Solution Phase Photocatalysis. *ACS Cent. Sci.* **2017**, *3*, 482−488.
(84) Zijlstra, P.; Orrit, M. Single Metal Nanoparticles: Optical Detection, Spectroscopy and Applications. *Rep. Prog. Phys.* **2011**, *74*, 106401.
(85) Weigel, A.; Sebesta, A.; Kukura, P. Dark Field Microspectroscopy with Single Molecule Fluorescence Sensitivity. *ACS Photonics* **2014**, *1*, 848−856.
(86) Chang, W. S.; Link, S. Enhancing the Sensitivity of Single-Particle Photothermal Imaging with Thermotropic Liquid Crystals. *J. Phys. Chem. Lett.* **2012**, *3*, 1393−1399.
(87) Parra-Vasquez, A. N. G.; Oudjedi, L.; Cognet, L.; Lounis, B. Nanoscale Thermotropic Phase Transitions Enhancing Photothermal Microscopy Signals. *J. Phys. Chem. Lett.* **2012**, *3*, 1400−1403.
(88) Ding, T. N. X.; Hou, L.; van der Meer, H.; Alivisatos, A. P.; Orrit, M. Hundreds-Fold Sensitivity Enhancement of Photothermal Microscopy in near-Critical Xenon. *J. Phys. Chem. Lett.* **2016**, *7*, 2524−2529.
(89) Rodriguez-Fernandez, J.; Perez-Juste, J.; Mulvaney, P.; Liz-Marzan, L. M. Spatially-Directed Oxidation of Gold Nanoparticles by Au(III)-CTAB Complexes. *J. Phys. Chem. B* **2005**, *109*, 14257−14261.
(90) Brongersma, M. L.; Halas, N. J.; Nordlander, P. Plasmon-Induced Hot Carrier Science and Technology. *Nat. Nanotechnol.* **2015**, *10*, 25−34.
(91) Zhang, Y. C.; He, S.; Guo, W. X.; Hu, Y.; Huang, J. W.; Mulcahy, J. R.; Wei, W. D. Surface-Plasmon-Driven Hot Electron Photochemistry. *Chem. Rev.* **2018**, *118*, 2927−2954.
(92) Kale, M. J.; Avanesian, T.; Christopher, P. Direct Photocatalysis by Plasmonic Nanostructures. *ACS Catal.* **2014**, *4*, 116−128.
(93) Linic, S.; Aslam, U.; Boerigter, C.; Morabito, M. Photochemical Transformations on Plasmonic Metal Nanoparticles. *Nat. Mater.* **2015**, *14*, 567−576.
(94) Besteiro, L. V.; Kong, X. T.; Wang, Z. M.; Hartland, G.; Govorov, A. O. Understanding Hot-Electron Generation and Plasmon Relaxation in Metal Nanocrystals: Quantum and Classical Mechanisms. *ACS Photonics* **2017**, *4*, 2759−2781.
(95) Hartland, G. V.; Besteiro, L. V.; Johns, P.; Govorov, A. O. What's So Hot About Electrons in Metal Nanoparticles? *ACS Energy Lett.* **2017**, *2*, 1641−1653.
(96) Wu, K.; Chen, J.; McBride, J. R.; Lian, T. Efficient Hot-Electron Transfer by a Plasmon-Induced Interfacial Charge-Transfer Transition. *Science* **2015**, *349*, 632−635.
(97) Minutella, E.; Schulz, F.; Lange, H. Excitation-Dependence of Plasmon-Induced Hot Electrons in Gold Nanoparticles. *J. Phys. Chem. Lett.* **2017**, *8*, 4925−4929.
(98) Kamarudheen, R.; Castellanos, G. W.; Kamp, L. P. J.; Clercx, H. J. H.; Baldi, A. Quantifying Photothermal and Hot Charge Carrier Effects in Plasmon-Driven Nanoparticle Syntheses. *ACS Nano* **2018**, *12*, 8447−8455.
(99) Zhou, L. A.; Swearer, D. F.; Zhang, C.; Robatjazi, H.; Zhao, H. Q.; Henderson, L.; Dong, L. L.; Christopher, P.; Carter, E. A.; Nordlander, P.; Halas, N. J. Quantifying Hot Carrier and Thermal Contributions in Plasmonic Photocatalysis. *Science* **2018**, *362*, 69−72.
(100) Wu, C. Y.; Wolf, W. J.; Levartovsky, Y.; Bechtel, H. A.; Martin, M. C.; Toste, F. D.; Gross, E. High-Spatial-Resolution Mapping of Catalytic Reactions on Single Particles. *Nature* **2017**, *541*, 511−515.
(101) Cortes, E.; Xie, W.; Cambiasso, J.; Jermyn, A. S.; Sundararaman, R.; Narang, P.; Schlucker, S.; Maier, S. A. Plasmonic Hot Electron Transport Drives Nano-Localized Chemistry. *Nat. Commun.* **2017**, *8*, 14880.
(102) Schlather, A. E.; Manjavacas, A.; Lauchner, A.; Marangoni, V. S.; DeSantis, C. J.; Nordlander, P.; Halas, N. J. Hot Hole Photoelectrochemistry on Au@SiO_2@Au Nanoparticles. *J. Phys. Chem. Lett.* **2017**, *8*, 2060−2067.
(103) Kim, Y.; Torres, D. D.; Jain, P. K. Activation Energies of Plasmonic Catalysts. *Nano Lett.* **2016**, *16*, 3399−3407.
(104) Smith, J. G.; Jain, P. K. The Ligand Shell as an Energy Barrier in Surface Reactions on Transition Metal Nanoparticles. *J. Am. Chem. Soc.* **2016**, *138*, 6765−6773.
(105) Burrows, N. D.; Lin, W.; Hinman, J. G.; Dennison, J. M.; Vartanian, A. M.; Abadeer, N. S.; Grzincic, E. M.; Jacob, L. M.; Li, J.; Murphy, C. J. Surface Chemistry of Gold Nanorods. *Langmuir* **2016**, *32*, 9905−9921.
(106) He, J.; Unser, S.; Bruzas, I.; Cary, R.; Shi, Z. W.; Mehra, R.; Aron, K.; Sagle, L. The Facile Removal of CTAB from the Surface of Gold Nanorods. *Colloids Surf., B* **2018**, *163*, 140−145.
(107) Ruijgrok, P. V.; Verhart, N. R.; Zijlstra, P.; Tchebotareva, A. L.; Orrit, M. Brownian Fluctuations and Heating of an Optically Aligned Gold Nanorod. *Phys. Rev. Lett.* **2011**, *107*, 037401.

DOI: 10.1021/acsnano.9b04702
ACS Nano 2019, 13, 12743−12757

(108) Trojek, J.; Chvatal, L.; Zemanek, P. Optical Alignment and Confinement of an Ellipsoidal Nanorod in Optical Tweezers: A Theoretical Study. *J. Opt. Soc. Am. A* **2012**, *29*, 1224−1236.
(109) Xu, X. H.; Cheng, C.; Zhang, Y.; Lei, H. X.; Li, B. J. Scattering and Extinction Torques: How Plasmon Resonances Affect the Orientation Behavior of a Nanorod in Linearly Polarized Light. *J. Phys. Chem. Lett.* **2016**, *7*, 314−319.
(110) Tong, L. M.; Miljkovic, V. D.; Kall, M. Alignment, Rotation, and Spinning of Single Plasmonic Nanoparticles and Nanowires Using Polarization Dependent Optical Forces. *Nano Lett.* **2010**, *10*, 268−273.
(111) Yan, Z. J.; Sweet, J.; Jureller, J. E.; Guffey, M. J.; Pelton, M.; Scherer, N. F. Controlling the Position and Orientation of Single Silver Nanowires on a Surface Using Structured Optical Fields. *ACS Nano* **2012**, *6*, 8144−8155.
(112) Yang, Y.; Saurabh, S.; Ward, J. M.; Nic Chormaic, S. High-Q, Ultrathin-Walled Microbubble Resonator for Aerostatic Pressure Sensing. *Opt. Express* **2016**, *24*, 294−299.
(113) Henze, R.; Seifert, T.; Ward, J.; Benson, O. Tuning Whispering Gallery Modes Using Internal Aerostatic Pressure. *Opt. Lett.* **2011**, *36*, 4536−4538.
(114) Cosci, A.; Quercioli, F.; Farnesi, D.; Berneschi, S.; Giannetti, A.; Cosi, F.; Barucci, A.; Conti, G. N.; Righini, G.; Pelli, S. Confocal Reflectance Microscopy for Determination of Microbubble Resonator Thickness. *Opt. Express* **2015**, *23*, 16693−16701.

DOI: 10.1021/acsnano.9b04702
ACS Nano 2019, 13, 12743−12757